

## Pulsar Observations II. – Coherent Dedispersion, Polarimetry, and Timing

I. H. Stairs

*National Radio Astronomy Observatory, P.O. Box 2, Green Bank, West Virginia 24944, USA*

**Abstract.** Pre-detection, or “coherent,” dedispersion is a powerful technique which completely eliminates the effects of dispersive smearing on pulsar profiles, greatly increasing the precision of timing and polarization observations. Various software and hardware implementations of this method are described. Polarization observations with filterbanks and with coherent dedispersion are discussed, including calibration and compensation for instrumental effects. Finally, the technique of pulsar timing is presented, with descriptions of the method for obtaining pulse times of arrival and the software used to fit models of the pulsar’s spin-down behavior, and a broad overview of scientific goals.

### 1. Introduction

Pulsar timing and polarization observations have a wide range of astrophysical applications, from studies of the internal structure of neutron stars, the pulsar radio emission mechanism, and the interstellar medium, to the exploration of binary evolution models, and stringent tests of general relativity and cosmological theories. The quality of all these experiments improves with increased signal-to-noise and, in the case of timing experiments, decreased pulse width. Conclusions regarding polarization are best drawn when the observed pulse profile most closely replicates the pulse shape emitted at the pulsar. This paper will discuss methods for obtaining the best possible timing and polarimetric signals and provide guidelines for their use.

### 2. Coherent Dedispersion

Pulsars are steep-spectrum objects, with signals typically strongest at observing frequencies of a few hundred MHz. At these frequencies, however, the pulses suffer significant dispersion as they propagate through the ionized interstellar medium (ISM). This phenomenon results in delays of lower-frequency components relative to the higher frequencies, and across a typical observing bandwidth can amount to hundreds or more times the pulse periods. The traditional method of dispersion removal has been a filterbank system, in which the bandpass is subdivided into a number of channels. The signal is detected in each channel, then shifted by the predicted dispersion delay in order to align the pulse peak (see Lecture by J. Cordes). However, far better timing and pulse-

profile precision can be achieved with the use of a coherent dedispersion system, in which the data are sampled before detection and dispersive smearing is completely removed (Hankins & Rickett 1975).

## 2.1. Principles

For the purpose of describing its effects on a propagating electromagnetic wave, the interstellar medium can be modeled as a low-density electron plasma, with plasma frequency

$$\nu_p = \sqrt{\frac{n_e e^2}{\pi m_e}}, \quad (1)$$

where  $n_e$  is the electron density,  $e$  the electron charge, and  $m_e$  the electron mass, all in cgs units. The wavenumber  $k(\nu)$  for radiation with frequency  $\nu$  can then be written as:

$$k(\nu) = \frac{2\pi}{c} \sqrt{\nu^2 - \nu_p^2}. \quad (2)$$

As the wave propagates, its phase is rotated by the ISM transfer function  $H(\nu) = e^{-ikz}$ , where  $z$  is the distance to the pulsar. This phase rotation causes the observed dispersive retardation.

For a filterbank, the frequency-dependent group velocity ( $v_g = 2\pi d\nu/dk$ ) can be used to determine the difference in pulse arrival times for two frequencies  $\nu_1$  and  $\nu_2$ :

$$t_1 - t_2 = \frac{e^2}{2\pi m_e c} \text{DM} \left( \frac{1}{\nu_1^2} - \frac{1}{\nu_2^2} \right), \quad (3)$$

where the dispersion measure, given by

$$\text{DM} = \int_0^d n_e dz, \quad (4)$$

is the integrated electron density along the line of sight to the pulsar, usually measured in  $\text{cm}^{-3} \text{pc}$ . This delay is the required relative shift of the detected signals in the two filterbank channels.

With coherent dedispersion, the raw telescope voltages are mixed to complex baseband signals using combinations of quadrature local oscillators, then sampled prior to detection. Dispersion removal then involves calculating the inverse of the ISM “chirp” function and convolving the time series with this new function. Using an approximate electron density of  $0.03 \text{ cm}^{-3}$  (Weisberg, Rankin, & Boriakoff 1980), the plasma frequency is estimated to be roughly 2 kHz, much smaller than both the typical observing frequency of several hundred MHz and the typical observing bandpass of order 10 MHz, and permitting a Taylor expansion of the wavenumber  $k(\nu)$ . For bandwidth  $B$ , we take  $\nu = \nu_0 + \nu_1$ , where  $\nu_0$  is the central observing frequency and  $|\nu_1| \leq B/2$ . Keeping only the first two terms in the expansion, we have:

$$k(\nu_0 + \nu_1) = \frac{2\pi}{c}(\nu_0 + \nu_1) \left[ 1 - \frac{\nu_p^2}{2(\nu_0 + \nu_1)^2} \right], \quad (5)$$

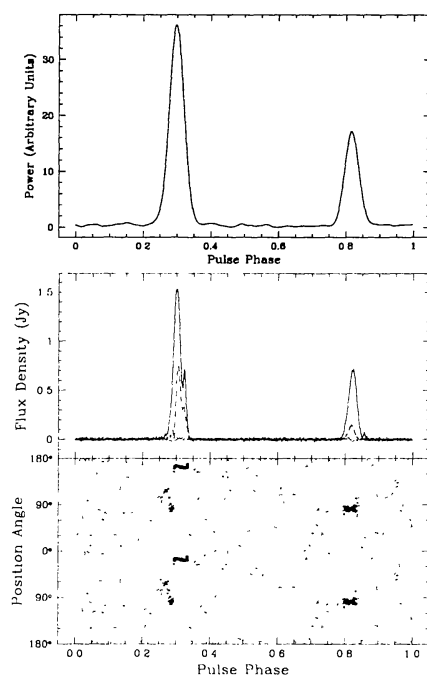


Figure 1. Pulse profile of the fastest rotating pulsar, PSR B1937+21, observed at 1400 MHz with the 76-m Lovell telescope at Jodrell Bank Observatory, U.K. The top panel shows the total-intensity profile derived from a filterbank observation; the true profile shape is convolved with the response of the channel filters. The lower panels show the full-Stokes observation with the Princeton “Mark IV” coherent dedispersion instrument (Stairs et al. 2000; Stairs, Thorsett, & Camilo 1999). Here, and in the following figures, total intensity is indicated by a solid line, linear intensity by a dashed line, and circular power by a dotted line. The position angle is plotted twice for clarity. (From Stairs 2001.)

which leads to the transfer function

$$H(\nu_0 + \nu_1) = \exp \left[ 2\pi i \frac{\text{DM}}{2.41 \times 10^{-10}} \frac{\nu_1^2}{\nu_0^2(\nu_0 + \nu_1)} \right], \quad (6)$$

for frequencies in MHz (see Hankins & Rickett 1975). Once the voltage time series has been convolved with the inverse of this function, the pulses are perfectly aligned in the time domain, and the data streams can be detected (squared) to yield high-precision profiles. If two polarizations are observed, suitable cross-products will yield the Stokes parameters, giving full polarimetric information. A comparison of filterbank and coherently dedispersed profiles for the 1.5-millisecond pulsar PSR B1937+21 is given in Figure 1.

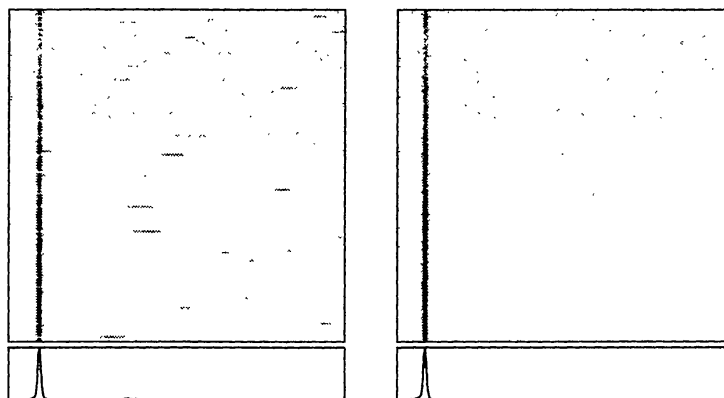


Figure 2. An example of broadband interference excision (Stairs et al. 2000). The left panel shows a grayscale plot of a contaminated 29-minute 610 MHz observation of PSR B1534+12 taken with the “Mark IV” instrument at Jodrell Bank. Each horizontal line represents ten seconds of data, and a cumulative pulse profile is displayed at the bottom. The broadband interference spikes have been “dedispersed” by roughly 6% of the pulse period, yielding the smeared-out bumps seen in the left-hand panel. The right panel presents the same observation, but with these broadband power spikes eliminated during processing.

## 2.2. Implementations

The coherent dedispersion method was pioneered more than 25 years ago (Hankins & Rickett 1975), but until recently, data storage and processing limitations resulted in mostly narrowband, hardware-based implementations with special-purpose chips performing the convolution of the data stream with the chirp function (e.g. Stinebring et al. 1992). These instruments and their more flexible, wider-bandwidth, modern digital counterparts (e.g. Backer et al. 1997; Kouwenhoven et al. 2000) operate by splitting the bandpass into narrow channels as in a filterbank, coherently dedispersing and detecting each channel, and then folding the data modulo the predicted topocentric pulse period. Such implementations allow the machines to cover large total bandwidths (100 MHz or more) and thereby produce high-signal-to-noise profiles. The primary disadvantage of a hardware implementation is that the data are recorded only after detection, making it impossible to reprocess with an improved dispersion measure, or to calculate and apply locally-relevant interference filters.

Software coherent dedispersion systems (e.g. Jenet et al. 1997; Weitfeldt et al. 1998; Stairs et al. 2000) trade wide total bandwidth for increased flexibility in processing. The instruments of the current generation do not subdivide the

observing bandpass, but instead mix the full signal (typically 10 MHz) to base-band and Nyquist-sample the entire passband, storing the sampled voltages on disk or tape for offline analysis.

Data analysis in software allows useful corrections and filters to be applied to the time series before the final data products are obtained. Coarse quantization (typically 2 bits) is often selected to keep the data rate manageable. This quantization will necessarily affect the observed pulse shapes and signal-to-noise ratios in statistically predictable ways. Accurate pulse profile shapes are needed for the determination of precise times-of-arrival (see Section 4.1.). Various schemes have been suggested to compensate for 2-bit quantization artifacts (Jenet & Anderson 1998; Stairs et al. 2000); these involve setting the quantization thresholds carefully relative to the root-mean-square input voltage, and re-spacing the floating-point numbers assigned to the quantization levels. Corrections for coarse quantization may be applied retroactively to the folded output of hardware systems.

Radio frequency interference is an increasingly important problem facing radio astronomy. Software dedispersion systems permit the calculation and application of filters in both the frequency and time domains, often with striking improvements to the profile baseline, pulse shape, and quality of the derived TOA. Figure 2 displays an example of time-domain, broad-band RFI excision. Such techniques can easily be extended beyond pulsar observations and may prove useful in many subfields of radio astronomy.

The total data volumes and storage requirements for recorder-style software systems quickly become very large: for an observing bandpass of 10 MHz, sampled with only 2-bit quantization, the resulting data rate is 10 MB/s, or 35 GB/hour. As the convolutions are generally performed using Fast Fourier Transforms, the processing requirements are also heavy, but with typical desktop computer speeds now the same order of magnitude as radio observing frequencies, affordable processing power is rapidly becoming less of a limitation. Future instruments, such as the planned COBRA instrument at Jodrell Bank, will likely include wide-bandwidth, multichannel machines with real-time software-based, rather than hardware-based, dedispersion. This will allow flexibility in interference excision and output mode (e.g. folded profiles or single-pulse time series) while eliminating most or all of the data storage requirement.

### 3. Polarimetry

Pulsars tend to be highly polarized, showing both circular and linear polarization, and with polarized fractions of up to 100%. Although the exact radio emission mechanism is poorly understood, a model which has achieved a certain amount of success is that of a rotating magnetic dipole. For a misaligned dipole, there will be a set of field lines above the polar caps which cannot close without forcing the plasma on these field lines to rotate at a speed above that of light (Goldreich & Julian 1969). The basic picture of radio emission then involves coherent radiation from charged particles streaming along these open field lines (Sturrock 1971). It was soon realized (Radhakrishnan & Cooke 1969,) that the position angle of linearly polarized emission from such a rotating dipole should follow a well-defined “S”-shaped curve, in what is known as the “rotating vector

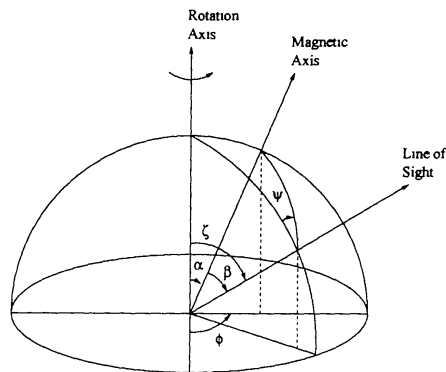


Figure 3. Definitions of angles in the Rotating Vector Model. The magnetic inclination is  $\alpha$  and the impact parameter is  $\beta$ . (After Manchester & Taylor 1977.)

model” (RVM). The geometry of the RVM is illustrated in Figure 3. The exact shape of the predicted curve depends on the inclination  $\alpha$  of the magnetic dipole axis relative to the spin axis and on the impact parameter  $\beta$  between the dipole axis and our line of sight. The position angle  $\psi$  can be written as a function of pulse phase  $\phi$ :

$$\tan(\psi(\phi) - \psi_0) = \frac{\sin \alpha \sin(\phi - \phi_0)}{\cos \alpha \sin(\zeta) - \sin \alpha \cos(\zeta) \cos(\phi - \phi_0)}, \quad (7)$$

where  $\zeta = \alpha + \beta$ ,  $\psi_0$  is a constant offset and  $\phi_0$  is the phase of steepest position-angle swing. A number of pulsars, particularly slow “young” ones such as the pulsar depicted in Figure 4, fit the RVM fairly well.

Pulsar polarimetry, in combination with the RVM and statistics of profile morphology, has led to phenomenological models of pulsar emission (e.g. Rankin 1983, 1990, 1993; Lyne & Manchester 1988), and has shown that such models do not seem to apply to millisecond pulsars (e.g. Xilouris et al. 1998; Stairs, Thorsett, & Camilo 1999). Determination of pulsar rotation measures leads to information about the magnetic field of our Galaxy (e.g. Han, Manchester, & Qiao 1999) and, on occasion, the magnetic field of a pulsar’s companion (Johnston et al. 1996). RVM fits can also be used to help constrain the orbital geometries of binary systems (e.g. Kramer 1998).

### 3.1. Data acquisition

Flux calibration of pulsar data is typically accomplished by pulsing an injected noise source, whose strength can be determined from comparison to a catalog flux calibration source. A typical procedure is to select a region of blank sky near the calibrator source, set the instrumental attenuation as for a normal observation, then pulse the noise calibrator signal and acquire data for a short time span. Subsequently, the telescope is moved to point at the calibrator, but the instrumental attenuation is not reset before acquiring more data. This allows



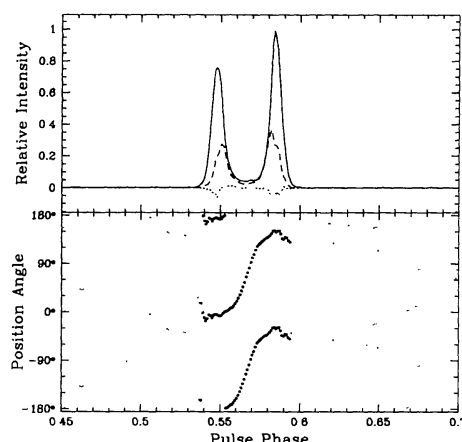


Figure 4. PSR B0525+21 observed at 1410 MHz with the 100-m telescope at Effelsberg, Germany (data from von Hoensbroech & Xilouris 1997). The position angle swing resembles the “S”-shaped curve expected from the Rotating Vector Model.

a direct comparison of the strength of the noise signal and the catalog source. If desired, small amounts of attenuation can be added or subtracted in order to test the overall linearity of the telescope/backend system. When observing a pulsar, it is only necessary to pulse the noise signal for a short time at the start or end of the observation in order to calculate the relative strengths of the pulsar signal and the noise source.

Assuming that left- and right-circular polarizations are observed and that some form of data cross-products are accumulated, it is straightforward to calculate the Stokes parameters:

$$I = |L|^2 + |R|^2, \quad (8)$$

$$Q = 2 \operatorname{Re}(L^* R), \quad (9)$$

$$U = 2 \operatorname{Im}(L^* R), \quad (10)$$

$$V = |L|^2 - |R|^2. \quad (11)$$

Hardware polarimeters are used with filterbank instruments. These fall into two categories: adding and multiplying polarimeters. Adding polarimeters are typically passive devices which sum the input voltages, in phase and rotated by  $90^\circ$ , producing outputs such as  $R$ ,  $L$ ,  $R + L$  and  $R + iL$  for input right- and left-circular polarizations. As the signals are not detected in the process, an adding polarimeter may be used before the signals are passed to the filterbank. Stokes parameters may then be calculated once the outputs have been filtered and detected. Multiplying polarimeters perform signal multiplication in hardware, typically yielding  $|R|^2$ ,  $|L|^2$ ,  $\operatorname{Re}(L^* R)$  and  $\operatorname{Im}(L^* R)$ ; a separate polarimeter must therefore be used for each filterbank channel. See von Hoensbroech & Xilouris

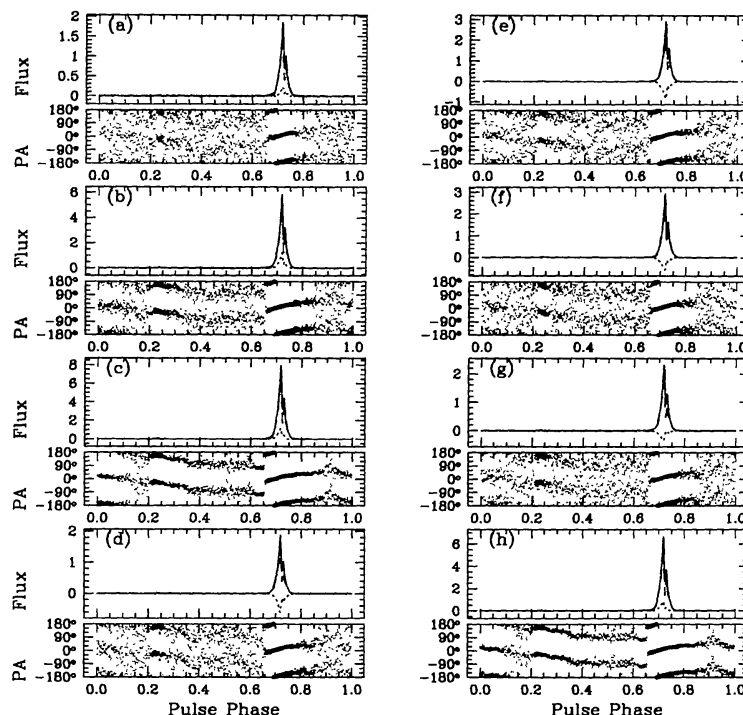


Figure 5. Arecibo observations of PSR B1929+10, uncorrected for the effects of antenna cross-coupling. Panels (a)–(g) are sequential 15- or 30-minute observations; panel (h) is cumulative. The circular polarization clearly changes shape and sign over the course of the observations, resulting in an incorrect cumulative profile.

(1997) for a thorough description of hardware polarimeter calibration at the Effelsberg 100-m telescope.

Correlator-style instruments produce self- and cross-product correlation functions after sampling the incoming voltages; the resultant data products are therefore similar to those produced by a filterbank plus multiplying polarimeter. See Navarro (1994) or the recently installed Wideband Arecibo Pulsar Processor (WAPP) instrument at Arecibo for examples.

Especially for fast, high-DM pulsars, coherent dedispersion offers a significant advantage over filterbank or correlator hardware systems. Coherent instruments produce profiles that, except for effects of interstellar scattering, exactly match those produced at the pulsar, and the Stokes parameters are quickly obtained by taking cross-products of the dedispersed time series.

### 3.2. Instrumental effects and corrections

For telescopes that are not equatorially mounted, the Stokes  $Q$  and  $U$  parameters are affected by the parallactic rotation of the feed during tracking. For a given hour angle, HA, telescope latitude  $\phi$  and source declination  $\delta$ , the parallactic



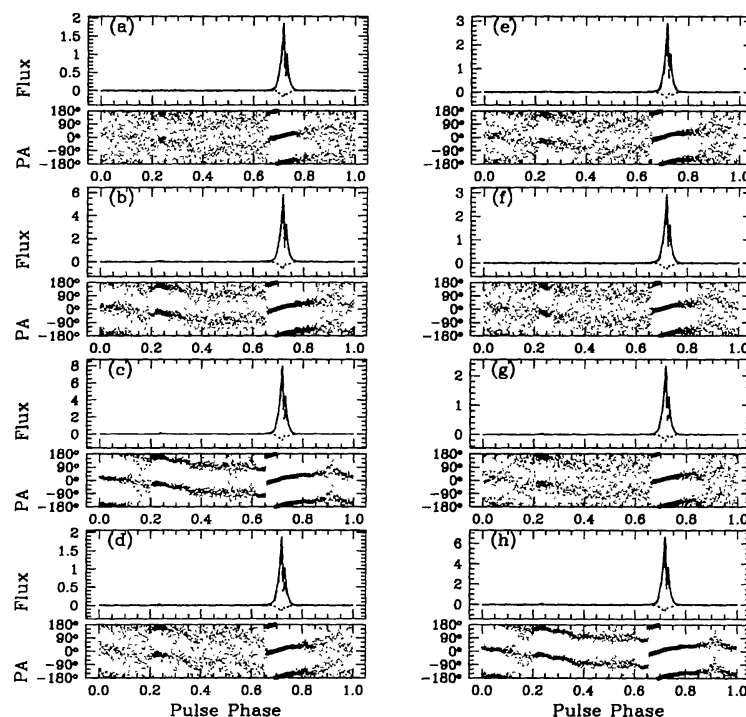


Figure 6. The same observations of PSR B1929+10 as in Figure 5, now corrected for the effects of antenna cross-coupling. Panels (a)–(g) are sequential 15- or 30-minute observations; panel (h) is cumulative. The circular polarization now maintains its intrinsic shape throughout the observing session.

angle  $\chi$  may be calculated by (Rankin, Campbell, & Spangler 1975):

$$\tan \chi = \frac{\sin HA \cos \phi}{\sin \phi \cos \delta - \cos \phi \sin \delta \cos HA}. \quad (12)$$

The correct parameters can be recovered by rotating the observed  $(Q_{\text{obs}}, U_{\text{obs}})$  pair by the angle  $-2\chi$ :

$$Q = Q_{\text{obs}} \cos(2\chi) - U_{\text{obs}} \sin(2\chi), \quad (13)$$

$$U = Q_{\text{obs}} \sin(2\chi) + U_{\text{obs}} \cos(2\chi). \quad (14)$$

The corrected  $Q$ ,  $U$  values may then be used to derive the linearly polarized power  $L$  and source position angle  $\psi$ .

$$L = \sqrt{Q^2 + U^2}, \quad (15)$$

$$\psi = \frac{1}{2} \tan^{-1}(U/Q). \quad (16)$$

A further complication arises from the fact that, in general, receiver antennas are not perfectly orthogonal, nor, in the case of “circular” antennas, perfectly responsive to circularly polarized radiation. This results in a mixing of the Stokes parameters, so that the observed Stokes vector is the product of the true Stokes vector and the so-called Mueller matrix, and can result in significant distortion of the pulse polarimetry. An example can be seen in Figure 5, in which a strongly linearly polarized pulsar was observed with nominally circular feeds on the 305-m Arecibo telescope. The distortion of the circular polarization as a function of time is evident.

It is possible to correct for this cross-coupling; in fact pulsars can be used to calculate the Mueller matrix for a receiver (Xilouris 1991). A first-order correction can be found following the method of Stinebring (1982), in which it is assumed that the circular antennas are orthogonal but elliptical. Then the most significant mixing effects are between  $L$  and  $V$ :

$$I' = I, \quad (17)$$

$$Q' = Q - V\epsilon_0 \cos \phi_0, \quad (18)$$

$$U' = U - V\epsilon_0 \sin \phi_0, \quad (19)$$

$$V' = V + L\epsilon_0 \cos(\theta - \phi_0), \quad (20)$$

where  $\theta$  is the incident position angle, and  $\epsilon_0$  and  $\phi_0$  are the cross-coupling parameters. For strongly linearly polarized pulsars such as PSR B1929+10, depicted in Figures 5 and 6, it is assumed that  $L_{\text{observed}} \simeq L$ . Then  $\epsilon_0$  and  $\phi_0$  can be determined by fitting a sinusoid to  $V'/L$  as a function of incident position angle;  $\epsilon_0$  and  $\phi_0$  may well vary somewhat across the observing bandpass. Once the cross-coupling parameters have been determined using a strong pulsar, they can be used to correct  $L$  and  $V$  for all pulsars observed with the same system. The corrected profiles from the Arecibo observations are displayed in Figure 6.

Stokes parameter mixing can also be induced by differences in path length from the antenna to the detector. This will mix  $Q$  and  $U$  for circular antennas, resulting in a measurable position angle offset, and  $U$  and  $V$  for linear antennas. In the latter case, the problem can be corrected by summing Stokes parameters taken with the antennas offset by a  $90^\circ$  rotation.

## 4. Pulsar Timing

Pulsars are among the most stable clocks in nature: some MSPs rival atomic clocks on timescales of several years (Rawley et al. 1987; Kaspi, Taylor, & Ryba 1994). High-precision timing requires two stages of analysis: determining the times of arrival (TOAs) of a set of pulses, and fitting a timing model to those TOAs.

### 4.1. Obtaining times of arrival (TOAs)

Although single pulses from any given pulsar fluctuate greatly in both intensity and shape, profiles representing the integrated waveform formed over several minutes are quite stable. This permits the accumulation of several hours' worth of data, at a given frequency and with a given observing system, to generate a "standard profile," against which any other profile may be cross-correlated.

During data acquisition and/or subsequent analysis, the data are folded modulo the predicted topocentric pulse period to form an integrated profile. The shape of this profile,  $p(t)$ , may be written as:

$$p(t) = a + bs(t - c) + g(t), \quad (21)$$

where  $s(t)$  is the standard profile,  $g(t)$  is gaussian noise,  $a$ ,  $b$  and  $c$  are constants, and  $0 \leq t \leq P$ , where  $P$  is the pulse period. Thus adding the time offset  $c$  to the time-stamp at the start of the integration yields the TOA. The constants  $a$ ,  $b$  and  $c$  may be found by least-squares fitting in the Fourier domain (for instance, using the FFTFIT routine, Taylor 1992) or in the time domain. It may be desirable to use the pulsar's polarization information (for example, a steep position-angle swing) to help determine the time offset  $c$ . TOA precision depends on the pulse strength and width and pulse-to-pulse stability, and is affected by many of the interstellar propagation effects discussed in the lecture by J. Cordes, such as scintillation, scatter broadening, and DM variations.

The most stable MSPs have period derivatives on the order of  $10^{-17} \text{ ss}^{-1}$  or smaller. Thus the best possible time standards must be used as references for the TOAs. The most commonly used time standard is Universal Coordinated Time (UTC), which is defined to be 1) an integral number of seconds from International Atomic Time (TAI), a weighted average of nearly 200 atomic clocks which is maintained by the Bureau International des Poids et Mesures (BIPM), and 2) never more than 0.9 s from UT1, the timescale defined by the rotation of the Earth. Leap seconds must occasionally be inserted into UTC in order to fulfill the second requirement, though it is possible that these may be eliminated in the next few years. A "real-time" version of UTC is readily accessible via broadcasts from the Global Positioning System (GPS) satellite array, and can be corrected retroactively. For the highest precision long-term timing (e.g. Kaspi et al. 1994), it is desirable to use TT ("Terrestrial Time"), which is specified relative to TAI, and is intended to represent the idealized geocentric timescale (Seidelmann, Guinot, & Doggett 1992). This retroactive time standard can be obtained from the BIPM as TT(BIPM). During observations, the data are given timestamps relative to the observatory's local time standard, often hydrogen masers. These timestamps are then corrected retroactively to UTC or TT(BIPM).

#### 4.2. The spin-down model

The rotating magnetic dipole model is also vital to pulsar timing, providing the expectation that the pulsar will lose energy and therefore “spin down” over the long term. This effect is measurable via a slow decrease in the pulse spin frequency. To model this spin-down, the pulse phase  $\phi$  may be written as a Taylor series in frequency:

$$\phi(T) = \phi(0) + \nu T + \frac{1}{2}\dot{\nu}T^2 + \frac{1}{6}\ddot{\nu}T^3 + \dots, \quad (22)$$

where  $T$  is time in the pulsar rest frame and  $\nu = 1/P$  is the pulse frequency. In practice, the frequency,  $\nu$ , and its first derivative,  $\dot{\nu}$ , are measurable for all pulsars, but the second derivative,  $\ddot{\nu}$ , is measurable only for young, rapidly-decelerating pulsars.

#### 4.3. Transformation to the solar system barycenter

The pulse times of arrival are measured in the observatory reference frame. Before any modeling of the pulsar parameters can be attempted, these topocentric TOAs must be transformed to an inertial reference frame. Though the approximation is not perfect, the most convenient inertial frame to use is that of the solar system barycenter. This transformation is sufficient for isolated pulsars; pulsars in binary systems require a further transformation to the pulsar frame, and more extensive parametrization.

A pulse arrival time  $t_b$  at the solar system barycenter is given by:

$$t_b = t + \frac{\mathbf{r} \cdot \hat{\mathbf{n}}}{c} + \frac{(\mathbf{r} \cdot \hat{\mathbf{n}})^2 - |\mathbf{r}|^2}{2cd} - \frac{D}{\nu^2} + \Delta_{E\odot} - \Delta_{S\odot}, \quad (23)$$

where  $t$  is the topocentric arrival time,  $\mathbf{r}$  is the vector from the barycenter to the telescope,  $\hat{\mathbf{n}}$  is a unit vector from the barycenter to the pulsar, and  $d$  is the barycenter-pulsar distance. The TOAs determined at observing frequency  $\nu$  are corrected to infinite-frequency values by the dispersion term,  $D/\nu^2$ . The dispersion constant,  $D$ , is related to the dispersion measure, DM, by  $D \equiv \text{DM}/(2.41 \times 10^{-16})$  Hz. The Einstein delay term,  $\Delta_{E\odot}$ , consists of gravitational redshift and time dilation effects due to the Sun, planets and other objects in the solar system. The Shapiro delay,  $\Delta_{S\odot}$ , describes the bending of spacetime in the potential well of the Sun; its maximum magnitude is about  $120 \mu\text{s}$  at the limb of the Sun.

The vector  $\hat{\mathbf{n}}$  is determined in part by the pulsar’s position on the sky (right ascension  $\alpha$  and declination  $\delta$ ) and its proper motion ( $\mu_\alpha \equiv \dot{\alpha} \cos \delta$  and  $\mu_\delta \equiv \dot{\delta}$ ). The third term on the right-hand side of Equation 23 represents parallax due to the Earth’s orbit; it is measurable only for nearby millisecond pulsars (e.g. Kaspi et al. 1994; Toscano et al. 1999). The transformation presented in Equation 23 is accomplished by interpolating a solar system ephemeris; the Jet Propulsion Laboratory’s DE200 ephemeris (Standish 1990) is the one commonly used.

#### 4.4. Binary pulsars

In the case of a binary pulsar, additional parameters describing the binary orbit must be fit in order to translate a pulse from the center-of-mass frame of the

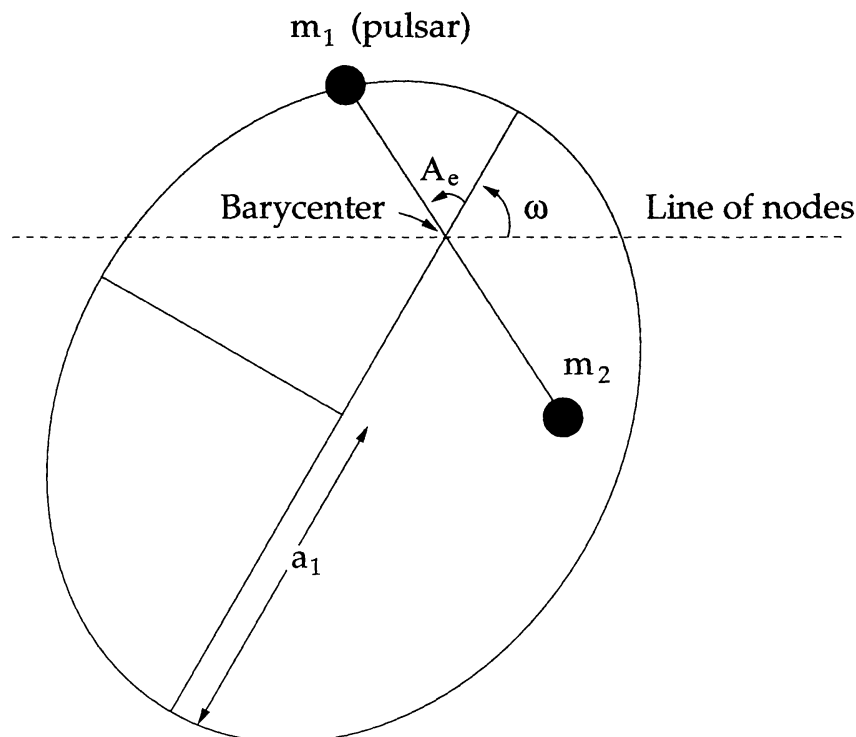


Figure 7. A binary pulsar orbit, with the line of nodes and definitions of the longitude of periastron,  $\omega$ , and the true anomaly,  $A_e$ , indicated.

binary (considered to be moving at constant velocity relative to the solar system barycenter) to the rest frame of the pulsar. For non-relativistic orbits, it is often sufficient to determine the five accessible Keplerian orbital parameters:  $x$ , the projected semi-major axis of the orbit;  $\omega$ , the longitude of periastron;  $T_0$ , the epoch of periastron;  $P_b$ , the orbital period; and  $e$ , the eccentricity, and to carry out the transformation on the basis of these values. For other systems, however, relativistic effects must be taken into account.

A complete “post-Newtonian” parametrization for binary systems was introduced by Damour & Deruelle (1986) and extended to include angular observables by Damour & Taylor (1992). It rewrites the orbital delay effects in terms of the five Keplerian parameters mentioned above and also a set of “post-Keplerian” parameters:  $\dot{\omega}$ , the advance of periastron;  $\dot{P}_b$ , the orbital period derivative;  $\gamma$ , the combined gravitational redshift and time dilation parameter;  $r$  and  $s$ , the “range” and “shape” of the Shapiro delay;  $A$  and  $B$ , the aberration parameters; and  $\delta_r$  and  $\delta_\theta$ , which represent orbital shape corrections. These parameters are defined in a theory-independent manner; the measured values may then be compared with the predictions of gravitational theories (e.g. Taylor & Weisberg 1989; Taylor et al. 1992; Stairs et al. 1998).

The resulting equation describing the transformation between the barycentric arrival time  $t_b$  and the corresponding time  $T$  in the comoving pulsar frame may be written as

$$T = t_b - \Delta_R - \Delta_E - \Delta_S - \Delta_A, \quad (24)$$

where  $\Delta_R$ ,  $\Delta_E$ ,  $\Delta_S$  and  $\Delta_A$  are the Roemer, Einstein, Shapiro and aberration delays across the pulsar orbit, defined by:

$$\Delta_R = x \sin \omega (\cos u - e(1 + \delta_r)) + x(1 - e^2(1 + \delta_\theta)^2)^{1/2} \cos \omega \sin u, \quad (25)$$

$$\Delta_E = \gamma \sin u, \quad (26)$$

$$\Delta_S = -2r \ln \left\{ 1 - e \cos u - s \left[ \sin \omega (\cos u - e) + (1 - e^2)^{1/2} \cos \omega \sin u \right] \right\} \quad (27)$$

$$\Delta_A = A[\sin(\omega + A_e(u)) + e \sin \omega] + B[\cos(\omega + A_e(u)) + e \cos \omega]. \quad (28)$$

These delays are written in terms of the eccentric anomaly  $u$  and true anomaly  $A_e(u)$ , and the time dependence of  $\omega$ , which are related by:

$$u - e \sin u = 2\pi \left[ \left( \frac{T - T_0}{P_b} \right) - \frac{\dot{P}_b}{2} \left( \frac{T - T_0}{P_b} \right)^2 \right], \quad (29)$$

$$A_e(u) = 2 \arctan \left[ \left( \frac{1+e}{1-e} \right)^{1/2} \tan \frac{u}{2} \right], \quad (30)$$

$$\omega = \omega_0 + \left( \frac{P_b \dot{\omega}}{2\pi} \right) A_e(u). \quad (31)$$

Figure 7 depicts the geometry of the binary system. The longitude of periastron,  $\omega$ , is defined relative to the line of nodes, where the pulsar's orbital plane intersects the plane of the sky. The orbital semi-major axis is  $a_1$ ; it is related to the projected semi-major axis  $x$  by:

$$x \equiv \frac{a_1}{c} \sin i, \quad (32)$$

where  $i$  is the angle between the line of sight and the orbital angular momentum. (An inclination of  $90^\circ$  implies that the the orbit is viewed edge-on.) It is apparent that the pulsar and companion masses are not among the measurable Keplerian parameters; however, using Kepler's third law, a "mass function" can be derived from the Keplerian observables:

$$f_1(m_1, m_2, i) \equiv \frac{(m_2 \sin i)^3}{(m_1 + m_2)^2} = x^3 \left( \frac{2\pi}{P_b} \right)^2 \left( \frac{1}{T_\odot} \right) M_\odot, \quad (33)$$

where  $T_\odot \equiv G M_\odot / c^3 = 4.925490947 \mu\text{s}$ ,  $M_\odot$  is the mass of the Sun, and  $m_1$  and  $m_2$  are in solar masses. For a typical pulsar mass of  $1.35 M_\odot$  (Thorsett & Chakrabarty 1999), the fact that  $\sin i \leq 1$  allows the mass function to be used to calculate a minimum possible companion mass.

If post-Keplerian parameters are measured, they may help to describe the geometry of the system more completely: for instance, in the theory of general relativity, the PK parameter  $s \equiv \sin i$ . Only for about 10 binary pulsar systems have any PK parameters been measurable.

Given the two-dimensional nature of astronomical measurements, there will always be an undetermined longitudinal velocity component to any timing solution. This amounts to a Doppler shift in the pulse period and, if applicable, the orbital period. This latter shift will change the system masses by a small fraction; however, as Damour & Deruelle (1986) point out, all instances of this Doppler-shift factor cancel out when calculating any expected orbital period derivative, thus it has no interesting impact on observable parameters.



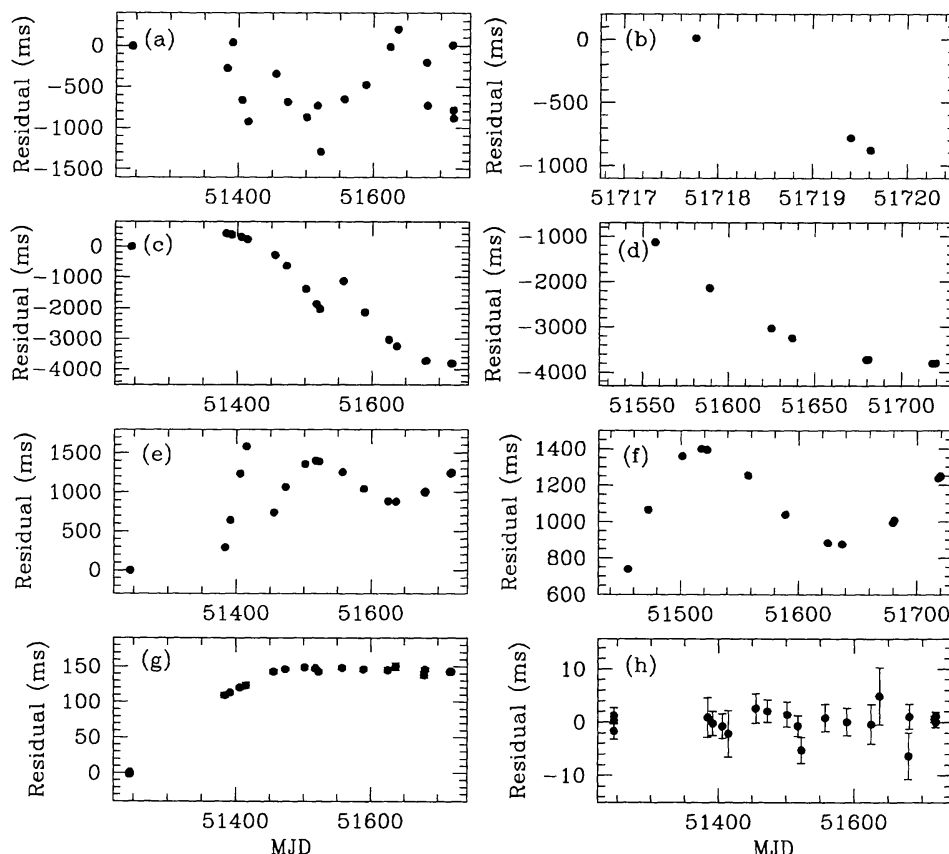


Figure 8. Obtaining a phase-connected solution for an isolated pulsar. (a) The scatter of residuals around the nominal initial solution consisting of the discovery parameters. The error bars are smaller than the plotted points. (b) Three closely-spaced points with no phase ambiguities are used to fit the frequency; the residuals relative to this new solution are in (c). (d) Adding more points allows a fit for frequency and frequency first derivative; residuals relative to such a fit are in (e). (f) A still-larger set of points containing a clear cubic term is selected, and the position terms are included in the fit. This solution leaves no phase ambiguities in the set of residuals in (g), and the fit may be extended to all points. (h) The final set of residuals; as the observations extend over more than a year, the position and spin parameters may be considered accurate.

#### 4.5. TEMPO

To fit the pulsar timing model to the data, many observers use the TEMPO program (Taylor & Weisberg 1989; see also <http://pulsar.princeton.edu/tempo>). This software package was written by J. Taylor in the 1970s, and has been continually evolving since, with major contributions from R. Manchester, D. Nice, J. Weisberg, A. Irwin and N. Wex. In brief, the program reads in a set of TOAs and an initial estimate of the timing parameters, then performs an iterative least-squares fit to the data in order to determine the improved timing parameters. In the process, it calculates the residual of each TOA relative to the timing model and the standard goodness-of-fit statistic,

$$\chi^2 = \sum_{i=1}^N \left( \frac{\phi(t_i) - n_i}{\sigma_i} \right)^2, \quad (34)$$

where  $\phi(t_i)$  is the measured pulse phase at time  $t_i$ ,  $n_i$  is the nearest integer pulse number and the uncertainty  $\sigma_i$  is in units of pulse phase. The success of the fitting algorithm depends on correctly numbering each individual pulse; once this is accomplished the solution is said to be “phase-connected.” Figure 8 demonstrates the fitting of a phase-connected solution for an isolated pulsar.

In practice, the art of pulsar timing requires careful examination of the post-fit residuals in order to check for any lingering systematics. The signatures of some problems are readily identifiable: for example, an incorrect proper motion will leave an annual sinusoidal curve that grows with time, while badly-fit orbital parameters will leave traces when the residuals are plotted against orbital phase. Ideally, the post-fit residuals should resemble random, gaussian noise and the  $\chi^2$  statistic should be close to the number of degrees of freedom. Finally, the accuracy with which the solution predicts arrival times should be tested against further observations; once all of these tests have been passed, the timing solution may be adopted with confidence. The TEMPO program can then be used to generate Chebyshev polynomial coefficients which will predict the pulsar’s spin phase over a limited range of time. This feature is valuable for creating the folded timing-observation profiles needed to refine the spin-down model.

#### 4.6. Starting points for science

With the assumption of purely dipolar radiation from an orthogonal rotator, measurement of a pulsar’s  $\nu$  and  $\dot{\nu}$  leads directly to an estimate of the surface magnetic field  $B$ :

$$B = \left( \frac{-3I\dot{\nu}c^3}{8\pi^2 R^6 \nu^3} \right)^{1/2} \approx 3.2 \times 10^{19} \left( \frac{-\dot{\nu}}{\nu^3} \right)^{1/2} G, \quad (35)$$

where  $R$  is the radius of the neutron star, about  $10^6$  cm, and the moment of inertia  $I = (2/5)1.4 M_\odot R^2 \approx 10^{45} \text{ g cm}^2$ .

It is often assumed that the loss of rotational energy will cause the pulsar spin frequency to evolve according to  $\dot{\nu} \propto -\nu^n$ , where the “braking index”,  $n$ , will be exactly 3 for magnetic dipolar radiation. The braking index can be calculated if the frequency second derivative is measured; the few successful such

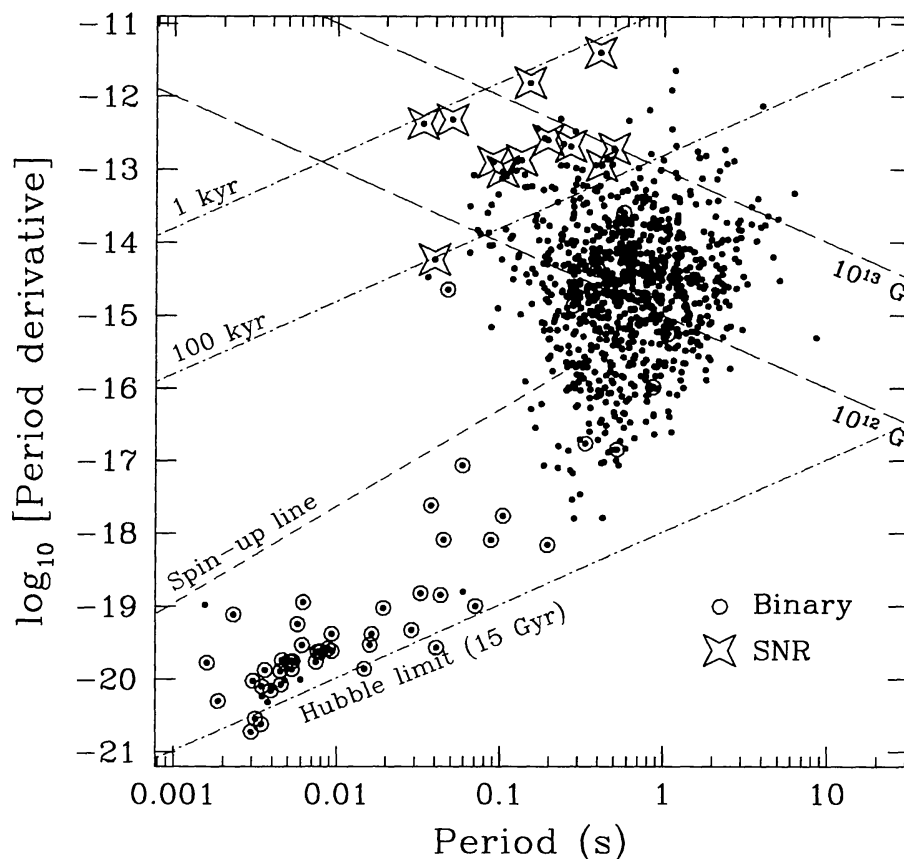


Figure 9. The  $P - \dot{P}$  diagram for Galactic field pulsars. Pulsars associated with supernova remnants are indicated by stars; those in binary systems by circles.

measurements have yielded braking indices less than 3 (e.g. Lyne, Pritchard, & Smith 1988), indicating some level of departure from the simple dipole approximation.

The spin-down model also allows an estimate of the age of the pulsar. For constant  $n$  and an initial spin frequency  $\nu_0$ , the age  $\tau$  is:

$$\tau = \frac{-1}{(n-1)} \frac{\nu}{\dot{\nu}} \left[ 1 - \left( \frac{\nu}{\nu_0} \right)^{n-1} \right]. \quad (36)$$

With the assumption of a very large initial spin frequency and constant magnetic dipolar braking ( $n = 3$ ),  $\tau_c$  becomes an upper limit to the pulsar's age:

$$\tau_c = -\frac{\nu}{2\dot{\nu}}. \quad (37)$$

The age and magnetic field of an individual pulsar are most useful when looked at in the context of the entire known pulsar population. A qualitative understanding of the population may be achieved by plotting  $\dot{P}$  against  $P$  on a logarithmic scale. Figure 9 does this for all known pulsars in the field of the Galaxy. (Though pulsars abound in globular clusters, the measured period derivatives of these pulsars are subject to bias from acceleration in the cluster potential.) Lines of constant age and constant magnetic field are also shown. The bulk of the population has spin periods of roughly 1 s and magnetic fields of the order of  $10^{12}$  G. Several of the youngest pulsars have solid or plausible associations with supernova remnants, consistent with accepted ideas about the formation of pulsars in supernova explosions. These young pulsars age, passing through the densest region of the diagram, and eventually reach the point at which the radio emission mechanism no longer functions. A “dead” pulsar lucky enough to have a main-sequence binary companion will be “spun up” through accretion of matter and angular momentum as the companion evolves, and may be resurrected with a smaller magnetic field and much faster spin period. The recycled and millisecond pulsars in the lower left corner of the diagram were produced in this manner. It is clear from the distribution on this diagram that the pulsar population displays a great diversity, and our understanding of the population and evolutionary processes will be much enhanced by the timing of new pulsars from current and future generations of surveys.

**Acknowledgments.** The data for the profile in Figure 4 were obtained from the European Pulsar Network data archive. Figure 2 is copyright R.A.S. 2000. The author is supported by an NRAO Jansky fellowship. She thanks Michael Kramer and Jim Cordes for reading the manuscript.

## References

- Backer, D. C., Dexter, M. R., Zepka, A., Ng, D., Werthimer, D. J., Ray, P. S., & Foster, R. S. 1997, *PASP*, 109, 61
- Damour, T. & Deruelle, N. 1986, *Ann. Inst. H. Poincaré (Physique Théorique)*, 44, 263
- Damour, T. & Taylor, J. H. 1992, *Phys. Rev. D*, 45, 1840
- Goldreich, P. & Julian, W. H. 1969, *ApJ*, 157, 869
- Han, J. L., Manchester, R. N., & Qiao, G. J. 1999, *MNRAS*, 306, 371
- Hankins, T. H. & Rickett, B. J. 1975, in *Methods in Computational Physics* Volume 14 — Radio Astronomy (New York: Academic Press), 55
- Jenet, F. A. & Anderson, S. B. 1998, *PASP*, 110, 1467
- Jenet, F. A., Cook, W. R., Prince, T. A., & Unwin, S. C. 1997, *PASP*, 109, 707
- Johnston, S., Manchester, R. N., Lyne, A. G., D’Amico, N., Bailes, M., Gaensler, B. M., & Nicastro, L. 1996, *MNRAS*, 279, 1026
- Kaspi, V. M., Taylor, J. H., & Ryba, M. 1994, *ApJ*, 428, 713
- Kouwenhoven, M. L. A., van Haren, P. C., Driesens, D., Langerak, J. J., Beijaard, T. D., Voûte, J. L. L., Stappers, B. W., & Ramachandran, R. 2000, in *IAU Colloq. 177, Pulsar Astronomy – 2000 and Beyond*, ed. M. Kramer, N. Wex & R. Wielebinski (San Francisco: ASP), 279

- Kramer, M. 1998, *ApJ*, 509, 856
- Lyne, A. G. & Manchester, R. N. 1988, *MNRAS*, 234, 477
- Lyne, A. G., Pritchard, R. S., & Smith, F. G. 1988, *MNRAS*, 233, 667
- Manchester, R. N. & Taylor, J. H. 1977, *Pulsars* (San Francisco: Freeman)
- Navarro, J. 1994, PhD thesis, California Institute of Technology
- Radhakrishnan, V. & Cooke, D. J. 1969, *Astrophys. Lett.*, 3, 225
- Rankin, J. M. 1983, *ApJ*, 274, 333
- Rankin, J. M. 1990, *ApJ*, 352, 247
- Rankin, J. M. 1993, *ApJ*, 405, 285
- Rankin, J. M., Campbell, D. B., & Spangler, S. R. 1975, NAIC Report 46
- Rawley, L. A., Taylor, J. H., Davis, M. M., & Allan, D. W. 1987, *Science*, 238, 761
- Seidelmann, P. K., Guinot, B., & Doggett, L. E. 1992, in *Explanatory Supplement to the Astronomical Almanac*, ed. P. K. Seidelmann (Mill Valley, California: University Science Books), 39
- Stairs, I. H. 2001 in *ASP Conf. Ser.*, 248, *Magnetic Fields Across the Hertzsprung-Russell Diagram*, ed. G. Mathys, S. K. Solanki & D. T. Wickramasinghe (San Francisco: ASP), 587
- Stairs, I. H., Arzoumanian, Z., Camilo, F., Lyne, A. G., Nice, D. J., Taylor, J. H., Thorsett, S. E., & Wolszczan, A. 1998, *ApJ*, 505, 352
- Stairs, I. H., Splaver, E. M., Thorsett, S. E., Nice, D. J., & Taylor, J. H. 2000, *MNRAS*, 314, 459
- Stairs, I. H., Thorsett, S. E., & Camilo, F. 1999, *ApJS*, 123, 627
- Standish, E. M. 1990, *A&A*, 233, 252
- Stinebring, D. R. 1982, PhD thesis, Cornell University
- Stinebring, D. R., Kaspi, V. M., Nice, D. J., Ryba, M. F., Taylor, J. H., Thorsett, S. E., & Hankins, T. H. 1992, *Rev. Sci. Instrum.*, 63, 3551
- Sturrock, P. A. 1971, *ApJ*, 164, 529
- Taylor, J. H. 1992, *Phil. Trans. Roy. Soc. A*, 341, 117
- Taylor, J. H. & Weisberg, J. M. 1989, *ApJ*, 345, 434
- Taylor, J. H., Wolszczan, A., Damour, T., & Weisberg, J. M. 1992, *Nature*, 355, 132
- Thorsett, S. E. & Chakrabarty, D. 1999, *ApJ*, 512, 288
- Toscano, M., Britton, M. C., Manchester, R. N., Bailes, M., Sandhu, J. S., Kulkarni, S. R., & Anderson, S. B. 1999, *ApJ*, 523, L171
- von Hoensbroech, A. & Xilouris, K. M. 1997, *A&AS*, 126, 121
- Weisberg, J. M., Rankin, J. M., & Boriakoff, V. 1980, *A&A*, 88, 84
- Wietfeldt, R., Straten, W. V., Rizzo, D. D., Bartel, N., Cannon, W., & Novikov, A. 1998, *A&AS*, 131, 549
- Xilouris, K. M. 1991, *A&A*, 248, 323
- Xilouris, K. M., Kramer, M., Jessner, A., von Hoensbroech, A., Lorimer, D., Wielebinski, R., Wolszczan, A., & Camilo, F. 1998, *ApJ*, 501, 286